
This is an electronic reprint of the original article.
This reprint may differ from the original in pagination and typographic detail.

Bandaru, V.; Hoelzl, M.; Bergström, H.; Artola, F. J.; Särkimäki, K.; Lehnen, M.; the JOREK Team

Assessment of runaway electron beam termination and impact in ITER

Published in:
Nuclear Fusion

DOI:
[10.1088/1741-4326/ad50ea](https://doi.org/10.1088/1741-4326/ad50ea)

Published: 01/07/2024

Document Version
Publisher's PDF, also known as Version of record

Published under the following license:
CC BY

Please cite the original version:
Bandaru, V., Hoelzl, M., Bergström, H., Artola, F. J., Särkimäki, K., Lehnen, M., & the JOREK Team (2024). Assessment of runaway electron beam termination and impact in ITER. *Nuclear Fusion*, 64(7), 1-14. Article 076053. <https://doi.org/10.1088/1741-4326/ad50ea>

This material is protected by copyright and other intellectual property rights, and duplication or sale of all or part of any of the repository collections is not permitted, except that material may be duplicated by you for your research use or educational purposes in electronic or print form. You must obtain permission for any other use. Electronic or print copies may not be offered, whether for sale or otherwise to anyone who is not an authorised user.

PAPER • OPEN ACCESS

Assessment of runaway electron beam termination and impact in ITER

To cite this article: V. Bandaru *et al* 2024 *Nucl. Fusion* **64** 076053

View the [article online](#) for updates and enhancements.

You may also like

- [Effect of pressure profile on stochasticity of magnetic field in a conventional stellarator](#)
Yasuhiro Suzuki
- [Topology bifurcation of a magnetic flux surface in toroidal plasmas](#)
K Ida, T Kobayashi, S Inagaki et al.
- [Equilibrium effects on the structure of island divertor and its impact on the divertor heat flux distribution in Wendelstein 7-X](#)
S. Zhou, Y. Liang, A. Knieps et al.

Assessment of runaway electron beam termination and impact in ITER

V. Bandaru^{1,2}, M. Hoelzl^{2,*} , H. Bergström² , F.J. Artola³, K. Särkimäki⁴, M. Lehnen³ 
and the JOEKE Team^a

¹ Indian Institute of Technology Guwahati, Guwahati, Assam, India

² Max Planck Institute for Plasma Physics, Garching, Germany

³ ITER Organization, Route de Vinon-sur-Verdon—CS 90 046, 13067 St Paul Lez Durance Cedex, France

⁴ Aalto University, Espoo, Finland

E-mail: mhoelzl@ipp.mpg.de

Received 18 January 2024, revised 26 April 2024

Accepted for publication 28 May 2024

Published 12 June 2024



CrossMark

Abstract

The vertical motion and shrinking of the cold plasma column after a tokamak disruption leads to a natural decrease in the edge safety factor when most of the current is carried by runaway electrons (REs). Reaching a low edge safety factor can potentially cause a strong plasma instability. We present magnetohydrodynamic simulations of the termination of a post-disruption plateau-phase RE beam in ITER when the edge safety factor falls close to two. Growth of instabilities is observed to result in stochastization of the magnetic field and a prompt loss of REs. As RE impact must be mitigated in ITER, the effect of parameters that influence the final termination have been assessed. Higher background plasma resistivity is seen to cause larger mode magnitudes and stronger stochastization, leading to less remnant REs after the termination event. Lower ion-densities also project a qualitatively similar behavior although weaker in effect. Using computations from a wall collision model, the ensuing load distribution on the first-wall is also presented.

Keywords: runaway electrons, ITER, tokamak, disruption, benign termination, MHD, stochastic fields

(Some figures may appear in colour only in the online journal)

1. Introduction

Tokamak plasma discharges can get terminated abruptly due to the stochastization of the magnetic field caused by large scale magnetohydrodynamic (MHD) instabilities [9, 30]. During a disruption, the plasma loses a large fraction of its thermal

energy on a fast timescale of typically 1ms in the biggest existing devices like JET, which is referred to as a thermal-quench (TQ). This increases the electrical resistivity of the plasma by a few orders of magnitude, and in turn leads to a decay of the plasma current causing a current-quench (CQ). Under certain plasma conditions, the current quench can result in the simultaneous formation of a high-energy beam of relativistic runaway electrons (REs), that carry nearly all the plasma current, which can be a significant fraction of the pre-disruption current [10, 19, 29]. Uncontrolled loss of REs can result in localized deep melting of the plasma facing components [21, 24, 27], and potentially also in the damage of cooling pipes. While REs have caused damage in the past, they are not a serious issue in existing tokamak experiments. However, in fusion-grade tokamaks such as ITER and beyond, unmitigated RE

^a See Hoelzl *et al* 2021 (<https://doi.org/10.1088/1741-4326/abf99f>) for the JOEKE Team.

* Author to whom any correspondence should be addressed.



Original Content from this work may be used under the terms of the [Creative Commons Attribution 4.0 licence](https://creativecommons.org/licenses/by/4.0/). Any further distribution of this work must maintain attribution to the author(s) and the title of the work, journal citation and DOI.

beams could potentially cause significant structural damage and machine downtime. Therefore it is essential to assess the potential impact of REs in ITER and devise robust mitigation strategies.

Several RE mitigation strategies have been proposed in the recent years, most of which typically involve well timed massive injection of impurities and/or Deuterium into the plasma [6]. Potentially promising among them has been the massive injection of Deuterium into the plasma during the RE plateau phase, that led to benign terminations wherein negligible wall damage was observed [25, 26]. Benign terminations using such a strategy were reported in several devices including JET, DIII-D, AUG and TCV [15]. The main goal of the present work is to assess the feasibility of benign terminations in ITER. While several factors play a role in such benign terminations, an eventual fast MHD crash has been a common feature observed, that is understood to cause distributed RE loads on the first-wall. At the same time, Deuterium injection is understood to cause a flushout of impurities, which ensures that any remnant RE population after such a crash does not re-avalanche efficiently. From the above discussion, it is clear that (a) an MHD instability, (b) drivers to ensure that the instability causes a strong enough crash, and (c) a deficiency of impurities in the plasma are the likely main ingredients in such benign terminations.

The MHD crash itself can be caused due to favorable conditions such as a hollow current density profile that is double-tearing-mode unstable or via a low edge safety factor (q_{95}). In ITER (and in any other device in general), a low value of q_{95} can in fact occur naturally during the RE plateau phase. This is attributed to two factors. The post TQ plasma invariably undergoes a vertical motion (cold VDE) causing a shrinking of the plasma minor radius (a). At the same time, REs are not subjected to resistive decay which ensures that the plasma current (I_p) does not vary significantly during the RE plateau phase. Due to the scaling $q_{95} \sim a^2/I_p$, the edge safety factor therefore effectively decreases. This is the main motivation of the present work, wherein we use non-linear 3D MHD simulations to investigate whether such a plausible low q_{95} condition in ITER can cause a crash and RE beam termination. The non-linear MHD code JOREK [7, 13, 17] including a RE fluid model [2] is used for this purpose. In addition, a high resistivity and/or a low ion-density are possible drivers in ensuring that an MHD unstable state actually ends up in a crash and a near-complete loss of REs. This is important due to the fact that both resistivity as well as ion-density will be modified by Deuterium injection. Therefore we also investigate the individual effects of resistivity and ion-density on the termination, in view of assessing if the Deuterium SPI scheme can work in ITER similar to how it seems to work in the existing devices. Finally, whether a termination event of such nature is benign or not depends on the actual deposition pattern on the first wall surface. This is assessed via test particle tracing and a wall collision model.

The paper is organized as follows. In section 2, the RE fluid model in JOREK used in this work is described briefly, followed in section 3 by a description of the simulation setup and starting state of the 3D simulations. In section 4, the results of the simulations are discussed including the effects of resistivity, ion-density; and also the wall loading. This is followed by a summary of the main conclusions and a brief outlook in section 5.

2. RE fluid and MHD model

For the present simulations, we use a reduced MHD model in the JOREK code with the inclusion of impurities and RE fluid. The magnetic field (\mathbf{B}), electric field (\mathbf{E}) and the ion-fluid velocity (\mathbf{v}) are respectively expressed as

$$\mathbf{B} = \frac{1}{R} \nabla \psi \times \mathbf{e}_\phi + \frac{F_0}{R} \mathbf{e}_\phi \quad (2.1)$$

$$\mathbf{E} = -F_0 \nabla u - \frac{1}{R} \partial_t \psi \quad (2.2)$$

$$\mathbf{v} \approx -R \nabla u \times \mathbf{e}_\phi \quad (2.3)$$

where ψ is the poloidal magnetic flux, R is the major radial coordinate, \mathbf{e}_ϕ is the unit vector in the toroidal direction and $F_0 u$ is the electric potential (with $F_0 = R_0 B_{\phi 0}$ being the major radius at the geometric center times the vacuum toroidal magnetic field). We neglect the parallel velocity of background ions and impurities ($v_{\parallel} = 0$) in this specific study. Comprehensive details of the reduced MHD models in JOREK can be found in [13]. Impurities are considered as a separate fluid and their density (ρ_{imp}) is evolved via $\mathbf{E} \times \mathbf{B}$ advection, along with diffusive transport and volumetric source as necessary. A coronal equilibrium model is used to obtain the charge state distribution of the impurities as a function of the background plasma properties. Furthermore, the temperatures encountered in our simulations do not go significantly below $\sim 2\text{eV}$, and hence the fraction of neutrals is negligible. In view of this, we do not track Deuterium neutrals in the present simulations,

$$\frac{1}{R^2} \frac{\partial \psi}{\partial t} = \frac{\eta}{R^2} \left(j - c \frac{F_0}{BR} n_r \right) - \frac{1}{R} [u, \psi] - \frac{F_0}{R^2} \frac{\partial u}{\partial \phi} - \frac{\eta_h}{R} \nabla^2 \left(\frac{j}{R} \right) \quad (2.4)$$

$$\begin{aligned} \nabla \cdot \left[\rho R^2 \nabla_{\perp} \frac{\partial u}{\partial t} \right] &= \frac{1}{2R} \left[R^2 |\nabla_{\perp} u|^2, R^2 \rho \right] + \frac{1}{R} \left[R^4 \rho \omega, u \right] \\ &\quad - \frac{1}{R} [j, \psi] - \frac{F_0}{R^2} \frac{\partial j}{\partial \phi} - \frac{1}{R} \left[R^2, \rho T \right] + R \mu \nabla^2 \omega \end{aligned} \quad (2.5)$$

$$j = \Delta^* \psi \quad (2.6)$$

$$\omega = \nabla \cdot (\nabla_{\perp} u) \quad (2.7)$$

$$\begin{aligned} \frac{\partial \rho}{\partial t} &= R [\rho, u] + 2\rho \partial_z u + \nabla \cdot \left[D_{\parallel, D} \nabla_{\parallel} (\rho - \rho_{\text{imp}}) \right] \\ &\quad + D_{\perp, D} \nabla_{\perp} (\rho - \rho_{\text{imp}}) + \nabla \cdot \left[D_{\parallel, \text{imp}} \nabla_{\parallel} \rho_{\text{imp}} \right] \\ &\quad + D_{\perp, \text{imp}} \nabla_{\perp} \rho_{\text{imp}} + S_D + S_{\text{imp}} \end{aligned} \quad (2.8)$$

$$\begin{aligned} \frac{\partial p}{\partial t} = & R[p, u] + 2\gamma p \frac{\partial u}{\partial Z} + (\gamma - 1) \nabla \cdot [k_{\perp} \nabla_{\perp} T + k_{\parallel} \nabla_{\parallel} T] \\ & + (\gamma - 1) \frac{\eta}{R^2} \left(j - c \frac{F_0}{BR} n_r \right)^2 - (\rho + \beta_{\text{imp}} \rho_{\text{imp}}) \rho_{\text{imp}} L_{\text{rad}}(T_e) \\ & - (\rho + \beta_{\text{imp}} \rho_{\text{imp}}) (\rho - \rho_{\text{imp}}) L_{\text{rad, Dcont}} \end{aligned} \quad (2.9)$$

$$\begin{aligned} \frac{\partial \rho_{\text{imp}}}{\partial t} = & R[\rho_{\text{imp}}, u] + 2\rho_{\text{imp}} \partial_Z u + \nabla \cdot (D_{\parallel, \text{imp}} \nabla_{\parallel} \rho_{\text{imp}} \\ & + D_{\perp, \text{imp}} \nabla_{\perp} \rho_{\text{imp}}) + S_{\text{imp}} \end{aligned} \quad (2.10)$$

$$\frac{\partial n_r}{\partial t} = \nabla \cdot (D_{\parallel, \text{RE}} \nabla_{\parallel} n_r) + R[n_r, u] + 2n_r \partial_Z u + S_{\text{Aval}}. \quad (2.11)$$

The REs are treated as a separate fluid species and only their number density n_r is evolved. The momentum and pitch angle of the REs are not tracked in this model. The total current density is expressed as $\mathbf{j} = \mathbf{j}_{\text{th}} + \mathbf{j}_r = \mathbf{j}_{\text{th}} - ec n_r \hat{\mathbf{b}}$, where \mathbf{j}_{th} is the thermal current density, \mathbf{j}_r is the RE current density, n_r the RE number density, e the electron charge, c the speed of light and $\hat{\mathbf{b}}$ the unit vector along the magnetic field. Perpendicular transport of the RE fluid is modeled using $\mathbf{E} \times \mathbf{B}$ advection. For the parallel transport, modeling parallel advection at the speed of light would be computationally prohibitive. Therefore we use a large parallel diffusion as an adhoc to mimic the physical advection at the speed of light. As shown in our earlier studies [3], fast parallel diffusion captures the fast loss of REs along the stochastic field lines adequately. The RE source of relevance here is only the avalanche (since we start with a full RE beam), which is computed taking into account the effective critical electric field and the effects of bound electrons in the partially-ionized impurities [11, 12]. The RE fluid interacts with the background plasma electromagnetically via a current-coupling, meaning that only the thermal part of the current density is subjected to resistive decay in the generalized Ohm's law. This also reflects in the corresponding Ohmic heating term, wherein the RE current density would not contribute. It must be noted that RE fluid models are also used in other MHD codes like EXTREM and M3D-C1 [18, 20].

The set of governing equations solved in the normalized form are shown above (excluding hyperdiffusion and numerical stabilization terms for brevity), where η is the electrical resistivity of the background plasma, η_h is the hyper-resistivity, ω is the toroidal component of vorticity, ρ_{imp} is the impurity density, ρ is the total mass density including Deuterium ions and impurities and $\beta_{\text{imp}} = \frac{m_i}{m_{\text{imp}}} \langle Z_{\text{imp}} \rangle - 1$ (with $\langle Z_{\text{imp}} \rangle$ being the average impurity charge). In addition, L_{rad} is the impurity radiation (including line, recombination and Bremsstrahlung), $L_{\text{rad, Dcont}}$ is the continuous radiation due to Deuterium ions and S_{Aval} is the RE avalanche source. Details of normalization can be found in [2 and 13].

Consistent magnetic boundary conditions are applied through the standard boundary integral approach using Green's functions, which obviates the need to extend the simulation domain beyond the plasma region. Referred to as JOREK-STARWALL coupling [1, 14, 22], this approach also

enables the inclusion of the effect of various active and passive conducting structures surrounding the plasma. For the rest of the variables (non-magnetic), standard fixed boundary conditions have been used.

3. Simulation setup and starting plasma state

The starting state of an RE beam in the plateau phase and with $q_{95} \sim 2$ for the present 3D simulations have been obtained via a preceding 2D simulation. For the sake of brevity, we present only a brief description of the various phases of the 2D simulation. We start with the free-boundary equilibrium of an elongated ITER-like plasma with $I_p = 14.6$ MA and $T_{e, \text{core}} = 15$ KeV, including the active and passive conducting structures surrounding the plasma. The conducting structures included (via STARWALL coupling) are the inner and outer shells of the vacuum vessel, poloidal field coils, central solenoid, divertor inboard rail and the outer triangular support. The electrical resistivity of the vacuum vessel is taken to be $\eta_{\text{wall}} = 0.8 \times 10^{-6}$ Ωm and the thickness of each shell is 6cm. The geometry of the plasma and the conducting structures are shown in figure 1(a).

The plasma in equilibrium is first subjected to an artificial TQ with simultaneous current-profile flattening. The current-profile flattening is meant to mimic the flattening expected due to Alfvénic activity during the thermal quench, and is executed via a large hyperresistivity. At the end of this phase, the plasma cools down to $T_e \approx 20$ eV with a relatively flat current density profile. This was followed by a spatially uniform introduction (1st injection) of Neon and Deuterium ($\Delta n_{\text{Ne}} = 1.35 \times 10^{20} \text{ m}^{-3}$ and $\Delta n_{\text{D}} = 1.81 \times 10^{20} \text{ m}^{-3}$) and an RE seed of 0.1 A. This causes a simultaneous CQ and avalanche of the RE seed along with a natural upward vertical motion of the plasma (cold VDE), and eventually results in the formation of an RE-beam carrying a current of ≈ 9 MA. Note that a high Neon density is assumed here to study a pessimistic scenario with a relatively large RE beam formation. Note also that the introduction of impurities as well as the RE beam formation leads to further cooling of the plasma, due respectively to radiation and decay of Ohmic heating. At this point, the edge safety factor is still relatively large with $q_{95} \sim 3.5$. Therefore the 2D simulation is continued further, during which the edge safety factor decays until $q_{95} \sim 2$. At this point the simulation is switched to 3D, which represents the starting or initial state for the 3D simulations presented here. Clearly the initial plasma state for the 3D simulations has a total plasma current (equal to the RE current) of ≈ 9 MA and is already significantly displaced vertically. Profiles of the electron temperature, current density and safety factor, along with the plasma position at this instant are shown in figures 1(b) and (c), for three different q_{95} values of 1.8, 2.0 and 2.2 (different starting points for 3D simulations). The electron temperature is nearly spatially uniform at around $T_e \sim 2.5$ eV, and the current profile is hollow with mild peaking around $\psi_N \approx 0.55$.

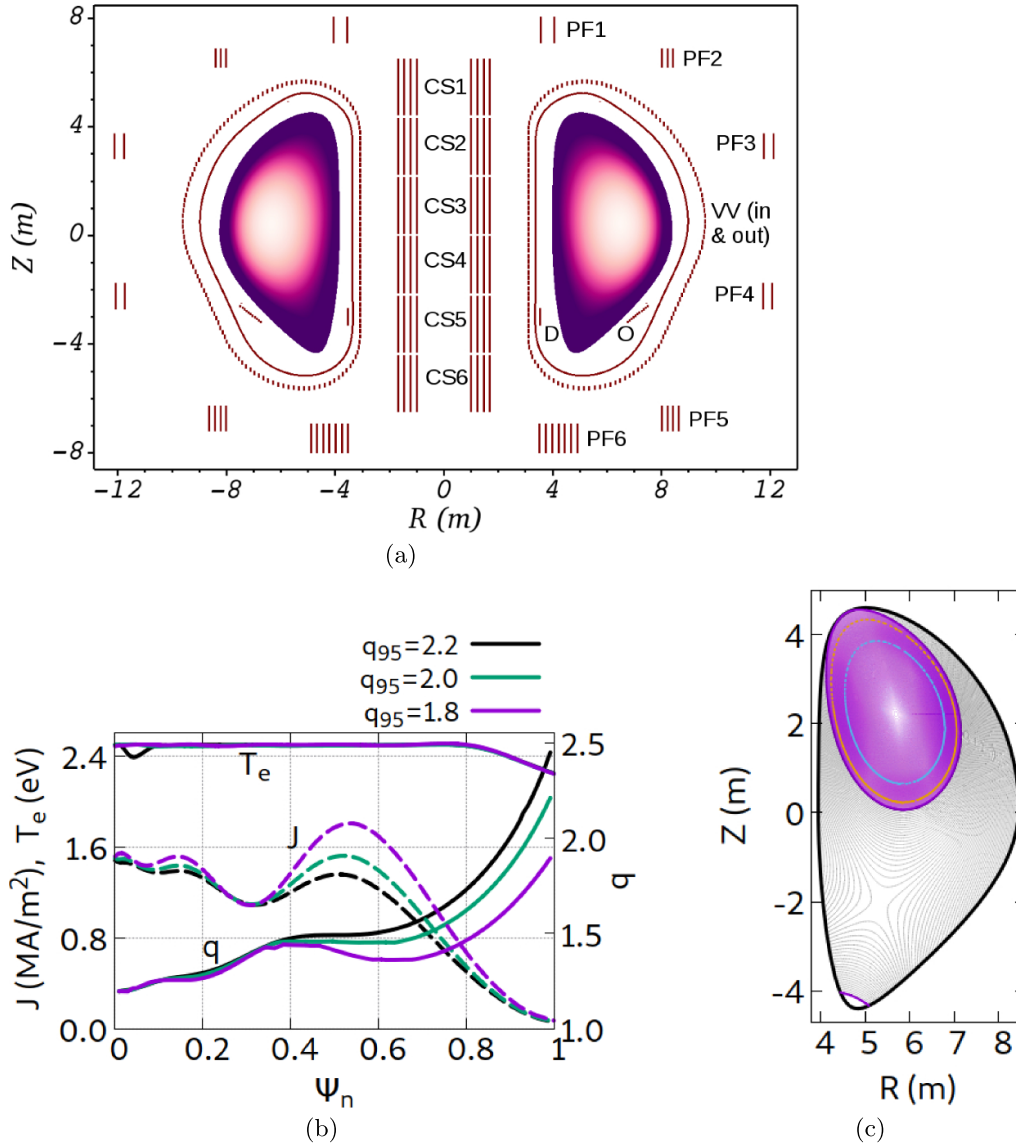


Figure 1. (a) Active and passive conducting structures of ITER used in the simulations via STARWALL (same for the preceding 2D simulation as well). The acronyms are VV: inner and outer shells of the vacuum vessel; PF: poloidal field coils; CS: central solenoid; D: divertor inboard rail; O: outer triangular support; Profiles of (b) Electron temperature, toroidal current density and safety factor, as a function of normalized poloidal magnetic flux ψ_N at the initial states from which the 3D simulations are started; (c) Plasma domain simulated in JOREK; domain boundary (black line), region with the last closed flux surface at the instant when 3D simulations are initiated (magenta), $q_{95} = 2.2$ case; the blue and orange curves represent the $q = 1.5$ and $q = 2$ rational surfaces respectively.

4. Simulation results

As mentioned earlier, when $q_{95} \sim 2$ is attained, a switch to 3D simulation is made along with a 3D noise level perturbation initialized in the plasma. The plasma electrical resistivity η is a function of electron temperature (T_e) and Z_{eff} , and is given by $\eta_{\text{sp}} = \eta_{\text{sp,c}} Z_{\text{eff}}$, where $\eta_{\text{sp,c}}$ is the classical Spitzer resistivity in the absence of impurities. The background plasma-fluid viscosity ($\mu = 5.2 \times 10^{-7} \text{ kg-m s}^{-1}$) is chosen to be temperature independent. To reduce computational costs for the simulations, RE parallel transport is modeled via a large parallel diffusivity $D_{\text{RE},\parallel} = 10^9 \text{ m}^2 \text{ s}^{-1}$ to mimic the fast parallel

advection. While the chosen value does not strictly correspond to transport at the speed of light, it ensures that the parallel transport timescale is far smaller than the tearing mode timescale. Numerical tests have shown that using a much larger value of parallel diffusivity can lead to spurious numerical perpendicular diffusion, which was the rationale for the present choice. Additionally, a small perpendicular diffusivity of $D_{\text{RE},\perp} = 4.6 \times 10^{-2} \text{ m}^2 \text{ s}^{-1}$ has been used for better numerical stability. A polar grid with radial and poloidal grid resolution $N_r \times N_\theta = 101 \times 128$ is used, along with toroidal modes $n = 0 \dots 5$. Sensitivity studies have shown that higher mode numbers $n = 6 \dots 10$ do not play a major role in the dynamics, as

Table 1. List of 3D MHD simulations performed. All 3D simulations here are based on the same 2D ITER simulation, which is an upward mitigated major disruption simulation obtained by an artificial thermal quench with current-flattening followed by Ne+D 1st injection and a subsequent RE avalanche. Simulations T1a, T1b and T1c were performed including modes $n = 0 \dots 3$ only, while the remaining simulations were performed including modes $n = 0 \dots 5$.

Run	q_{95}^{start}	note	$I_{\text{RE}}^{\text{init}}$ (MA)
T1a	1.8	—	9
T1b	2.0	—	9
T1c	2.2	—	9
T2a	2.2	<i>Baseline</i>	9
T3a	2.2	$\eta = 3x$	9
T3b	2.2	$\eta = 10x$	9
T4a	2.2	$n_i^D = 50\%$	9
T4b	2.2	$n_i^D = 15\%$	9
T4c	2.2	$n_i^D = 5\%$	9

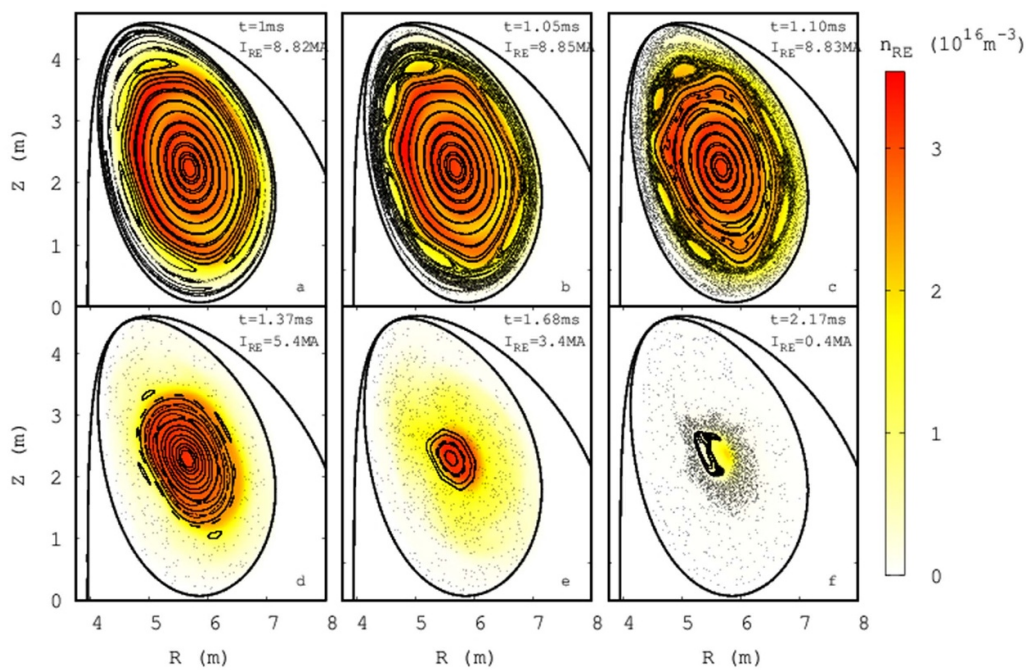


Figure 2. Poincaré plots over time for the baseline termination case T2a with $q_{95} = 2.2$. The color map represents the RE number density. The time instants corresponding to each panel is marked by vertical dashed lines with the same labels (a, b, c, d, e and f) in figure 3.

their individual mode energies are a factor of ~ 8 smaller compared to the dominant mode in the non-linear phase. Hence including $n = 0 \dots 5$ enables capturing the essential features at reduced computational costs.

In principle, the RE beam can become unstable much earlier than when $q_{95} \sim 2$. Nevertheless, performing 3D simulations over a long duration starting from say the early plateau phase is computationally expensive. We scanned over several values of starting q_{95} , which include among others, values of 2.2, 2.0 and 1.8 (this particular scan was done including only $n = 0 \dots 3$ modes). In all the cases, the plasma was found to be unstable. In addition, the dynamics and the overall theme of plasma evolution remained qualitatively similar in all these cases. In this paper, we therefore focus only on cases related to a starting $q_{95} = 2.2$. The list of all relevant cases have been summarized in table 1, which includes cases related to the

effect of resistivity and ion-density. The case T2a is considered to be the reference or baseline scenario for further discussion, which will be shown first.

After the 3D perturbation is initiated, there is an exponential growth of modes. The linear growth is marked predominantly by the toroidal mode numbers $n = 1$, $n = 2$ and $n = 4$, in specific dominated by the $(m, n) = (2, 1)$ and the $(m, n) = (6, 4)$, where m is the poloidal mode number. The 2/1 mode grows closer to the boundary, while the 6/4 is a double-tearing mode that grows due to the mildly hollow current profile. The corresponding rational surfaces can be seen from figure 1(c). From panel (a) of the Poincaré plots in figure 2, one can see the mode-structure slightly after the end of the linear-phase. One can observe the predominance of the 2/1 mode and the 6/4 double-tearing modes. It must be noted that both the hollow current profile as well as the lower edge safety factor

contribute to the overall evolution of the instabilities. Further growth of the 2/1 mode causes the stochasticization of the outer region close to the $q = 2$ surface (see panel (b) of figure 2). During this phase, the $(m, n) = (3, 2)$ mode energy grows to significance and starts to strongly impact the non-linear process. Following this, there is a marked transformation from a dominant 6/4 to a dominant 3/2 mode at the $q = 1.5$ surface. This is accompanied by a stochasticization of a significant portion of the outer region as shown in panel c) of figure 2. This happens over a time span of 1.1 ms from the time the 3D noise level perturbation is initiated, and the effect of RE parallel transport (and therefore an RE current drop) does not manifest yet. Further to this, the stochastic region continues to grow radially inward through a series of instabilities, while simultaneously losing RE current due to fast parallel transport. Gradients in RE density caused by the differential loss of REs between the closed-flux-surface and the stochastic region might play a role in the process of core-shrinking (see panels (d)–(f) of figure 2). The core-shrinking process (shrinking of the closed flux-surface or non-stochastic region) is reminiscent of the benign termination simulation of shot number 95135 in JET using JOREK as described in [3]. After a total duration of about 2.2 ms, only about 350 kA RE current survives in a small region near the core. The duration for RE termination quoted here refers to the time taken to reach an approximate minima in RE current. In fact the remnant RE current can re-avalanche and grow into a large beam again, aspects of which will be reported in detail elsewhere. The overall evolution of 0D quantities for this baseline scenario is shown in figure 3. One can observe that the $n = 1$ magnetic mode plays a dominant role in the later non-linear phase that causes core-shrinking. Perturbation in the poloidal magnetic field (computed as the ratio of the square root of energy of non-zero modes to total energy of poloidal magnetic field) reaches a peak magnitude of $\sim 8\%$ (see figure 3), while the electron temperature increases to a peak value ~ 6 eV (near the core) due to the reactivation of Ohmic heating as RE current is lost. The effect of Ohmic heating getting reactivated can be observed also via the increase in the plasma thermal energy shown in figure 3. We now turn to the effect of background plasma resistivity on the termination.

4.1. Effect of background plasma resistivity

Formation of an RE beam post a disruption leads to the current not being subjected to significant resistive decay and hence nearly no loss of magnetic energy via Ohmic heating. Lack of Ohmic heating and the presence of radiation due to impurities will cause the plasma electron temperature to drop to very low values of a couple of eV. This leads to the typical situation of RE beams in a highly resistive background plasma. Additionally, significant neutralization of background plasma can occur at such lower temperatures, in which case the resistivity can be dependent on electron-neutral collisions in addition to electron-ion collisions. This can increase the resistivity to even higher values and is the motivation for the present study wherein we intend to investigate if there is a fundamental

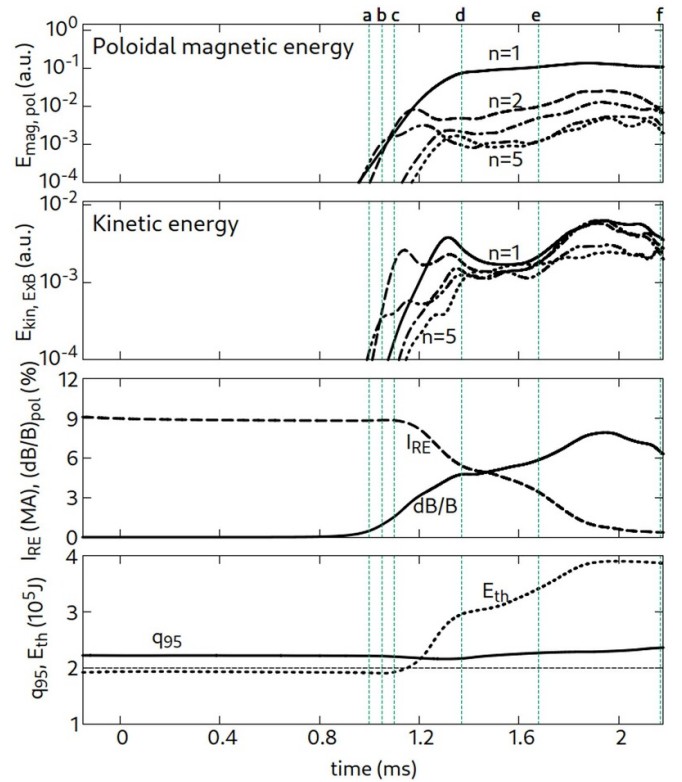


Figure 3. Global quantities for the termination case T2a (also referred to as the *Baseline* case) as a function of time. First panel (topmost): energy of the poloidal magnetic field in different toroidal modes; second panel: kinetic energy in different toroidal modes; third panel: RE current and normalized perturbation in poloidal magnetic field; fourth panel (bottommost): edge safety factor and plasma thermal energy. Vertical dashed lines labeled as a, b, c, d, e and f represent the time instants of the correspondingly labeled panels in figure 2.

difference to the MHD dynamics at higher resistivity. It must be mentioned that such an increased resistivity would not lead to a significant decay in RE current within the short timescale of the RE beam termination event investigated here. The effect of neutrals on the resistivity is not treated explicitly here, but rather the equivalent standalone effect of higher values of resistivity is investigated. Recently, [23] have investigated the effect of resistivity on the non-linear dynamics of a double-tearing mode in the classical case without REs.

Termination simulations at three different values of resistivity are compared (all starting with $q_{95} = 2.2$). They correspond to $\eta = 1.86 \times 10^{-4}$ Ohm.m (referred to as the *baseline* case), $\eta = 5.6 \times 10^{-4}$ Ohm.m (referred to as the $\eta = 3x$ case) and $\eta = 1.86 \times 10^{-3}$ Ohm.m (referred to as the $\eta = 10x$ case). Ohmic heating increases consistently when the resistivity is increased (of course this manifests only when REs are lost and some thermal current kicks in). In order to perform the higher resistivity simulations, a smooth parameter transition is made during the final phase of the 2D simulation, before the switch to 3D is made. Though the starting temperature (for 3D simulations) has a flat profile, the resistivity remains a function of temperature and effective ion-charge.

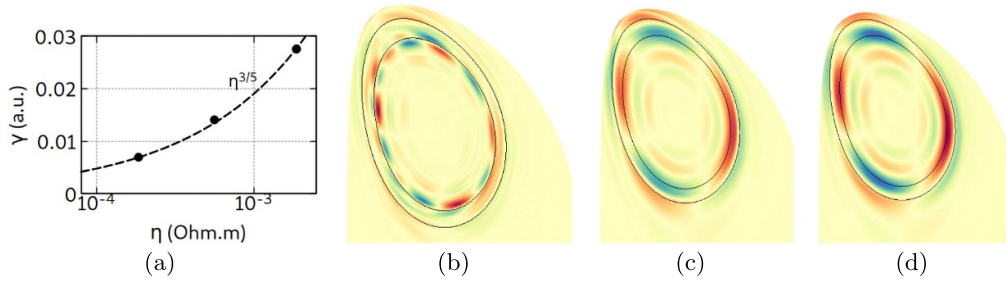


Figure 4. (a) Linear growth rate of the $n = 1$ mode versus the electrical resistivity. The dashed line indicate the $\tau_{\text{res}}^{-3/5}$ scaling. $n \neq 0$ perturbations of the toroidal current density close to the end of linear phase for (b) baseline case (T2a) at $t = 0.89$ ms; (c) $\eta = 3x$ case (T3a) at $t = 0.48$ ms and (d) $\eta = 10x$ case (T3b) at $t = 0.26$ ms. The color scale spans between -0.2 (red), yellow (0) to 0.2 (blue) for (b) and (c); and -0.26 (red), yellow (0) to 0.26 (blue) for panel (d) in JOREK units.

Note that only the resistivity is changed keeping all other parameters of the simulations identical in order to isolate the effects. As expected, the linear growth rate is larger at higher resistivity and the actual scaling for the $n = 1$ mode closely resembles the $\tau_{\text{res}}^{-3/5}$ or $\eta^{3/5}$ scaling (see figure 4(a)) for a tearing mode [8], where $\tau_{\text{res}} = \mu_0 L^2 / \eta$ is the resistive timescale (with L being the relevant length scale). However, there are strong differences in the mode structure and subsequent non-linear evolution at larger resistivity. The $n \neq 0$ perturbation of the current density near the end of the linear phase is compared in figures 4(b)–(d). Unlike the 2/1 plus 6/4 double-tearing modes that were dominant in the baseline case, at higher resistivity the effect of $q_{95} \sim 2.2$ and the mildly hollow profiles manifest as a dominant $m/n = 2/1$ tearing mode. Larger resistivity results in the mode becoming relatively wider (as compared to the baseline scenario), spanning significantly inward (radially) from the $q = 2$ surface. This is seen in both the higher resistivity cases as can be seen in figures 4(c) and (d). The 2/1 mode grows significantly in size and energy, and remains the predominant feature further into the non-linear phase, as can be seen from the blue and magenta curves in the top 3 panels of figure 5. Unlike the baseline scenario, the growth of the 2/1 mode to such a large magnitude can be attributed to the absence of significant non-linear interference from secondary modes, such as the stochasticization involving the 6/4 or 3/2. Such a mechanism was described in the work of [23] in the context of a double-tearing mode without REs.

Further into the non-linear phase, the field stochastizes in the outer region followed by core-shrinking eventually causing the entire field to stochastize. This is shown in the evolution of the Poincaré plots in figure 6. Due to the large magnitude of MHD in the higher resistivity cases, the stochasticization is rather strong and the RE current loss is nearly complete. At the end of the crash, the remaining RE current amounts to 26 kA and 13 kA respectively for the $\eta = 3x$ and $\eta = 10x$ cases, as compared to the 350 kA in the baseline scenario (see table 2). Enhanced stochasticization at higher resistivity can be substantiated by the magnitude of connection length. This is shown in figure 7, wherein the connection length is plotted as a function of the normalized time duration and normalized poloidal flux. Far shorter connection lengths are observed as the resistivity

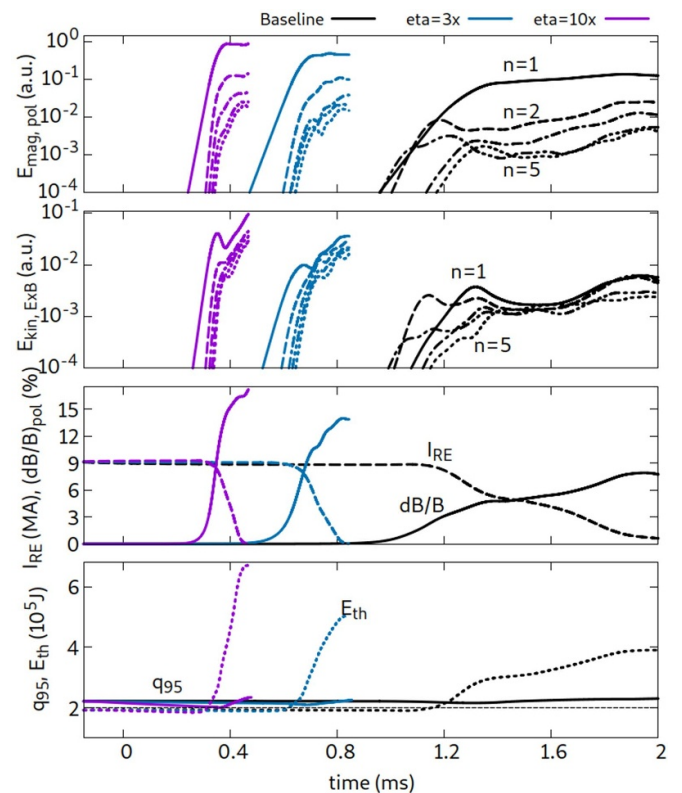


Figure 5. Comparison of global quantities for the terminations cases with different electrical resistivity. Baseline refers to case T2a, $\eta = 3x$ to T3a and $\eta = 10x$ to T3b.

is increased. Such strong dynamics at high resistivity might be potentially beneficial for benign RE beam termination in ITER, as we will see later in this paper.

4.2. Effect of ion-density

As mentioned earlier, plasmas with RE beams can neutralize significantly and hence can lead to low ion-densities, in turn leading to a faster Alfvén timescale ($\tau_A \sim \sqrt{\rho}$). Since tearing mode growth and MHD dynamics in general depend on the Alfvén timescale, it is of interest to understand the effect

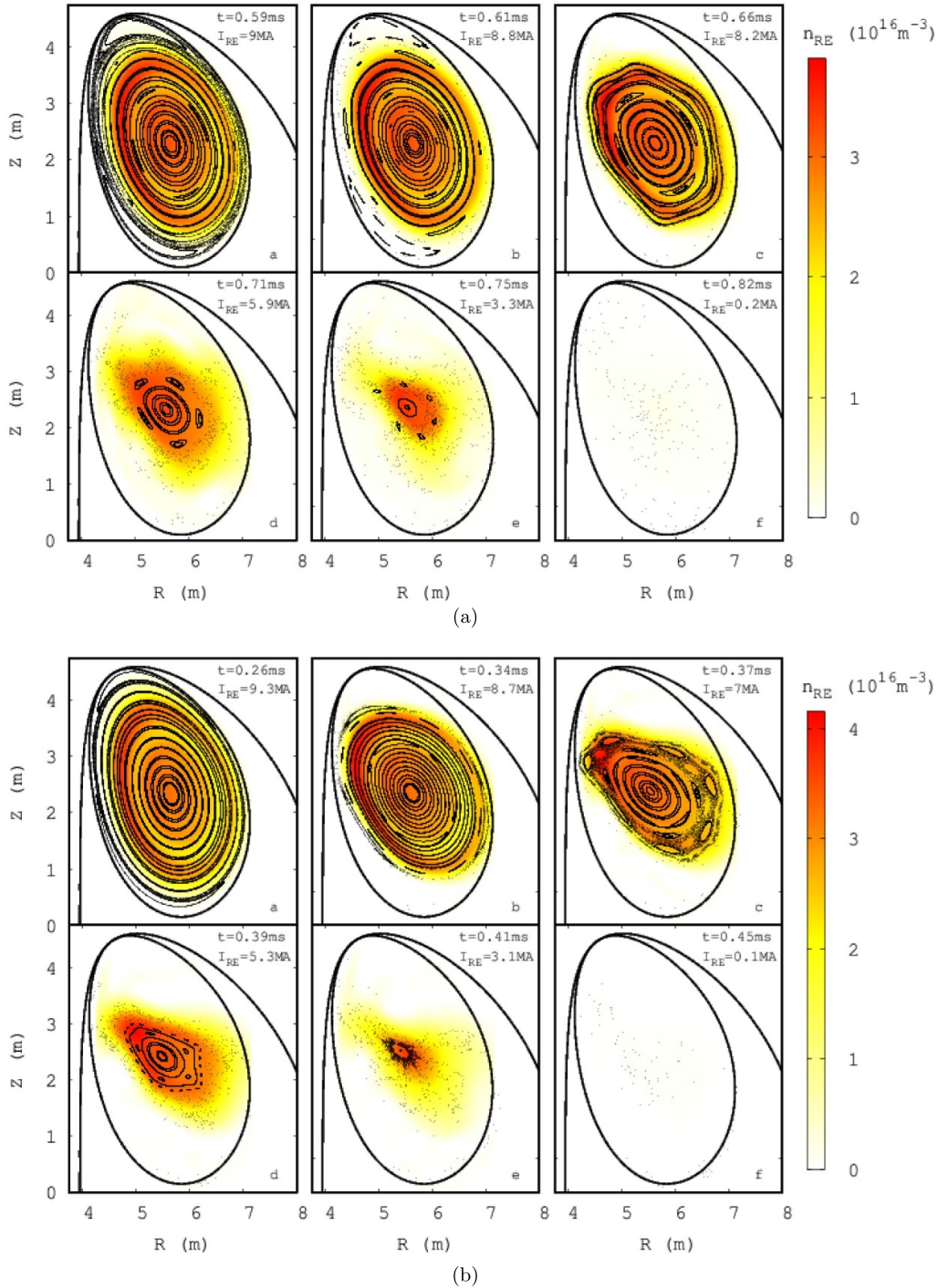


Figure 6. Poincaré plots over time for the termination cases (a) $\eta = 3x$ (T3a); (b) $\eta = 10x$ (T3b). Color map represents the RE number density.

of a decrease in ion-density on the RE termination scenarios. Importantly, recent experiments at TCV and AUG have shown a strong dependence of benign termination on the electron density via the quantity of injected Deuterium [28]. In this section, we investigate this aspect via simulations of RE termination at 50%, 15% and 5% of the baseline Deuterium ion-density. The Alfvén speed based on the Deuterium ion-density for the above three cases are respectively 2.3%, 4.2% and 7.2%

of the speed of light (when based on the total density, the difference in Alfvén speeds are not so stark). For even higher Alfvén velocities at lower densities, relativistic extensions of MHD might be required. The baseline case remains the same as in the previous subsection, i.e. Run T2a is compared to Runs T4a, T4b, and T4c. As was the case with studying the effect of resistivity, we concentrate on the isolated effect of decreasing the ion-density, while keeping all other parameters fixed.

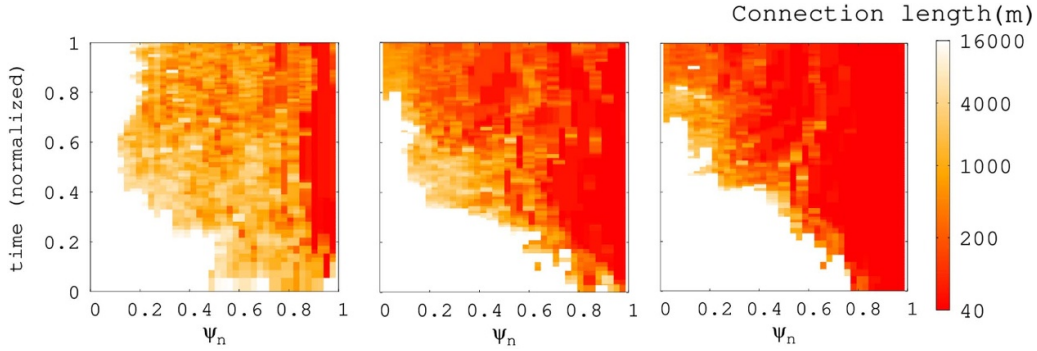


Figure 7. Evolution of field line connection length (colored) as a function of normalized poloidal flux ψ_N and normalized time. Time normalization is done individually over the total duration considered in each case, which is 0.97 ms, 0.221 ms, and 0.134 ms respectively for the baseline (T2a), $\eta = 3x$ (T3a) and $\eta = 10x$ (T3b) cases. Logscale is used for the colorbar.

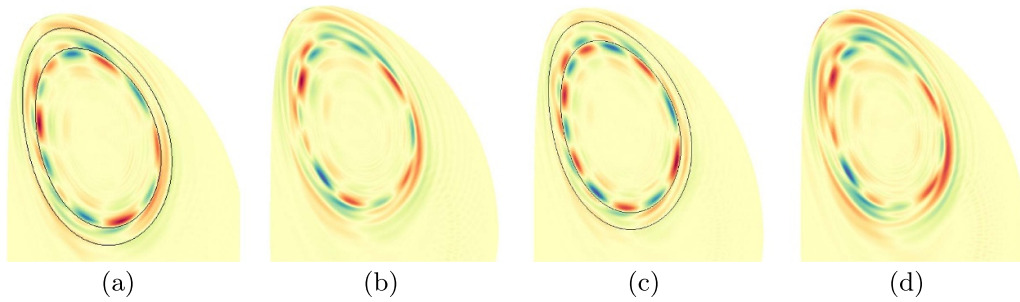


Figure 8. $n \neq 0$ perturbation of the toroidal current density close to the end of the linear phase for (a) baseline case; (b) $n_D^{\text{ion}} = 50\%$ case; (c) $n_D^{\text{ion}} = 15\%$ case and (d) $n_D^{\text{ion}} = 5\%$ case. The color scale spans between -0.2 (red), yellow (0) to 0.2 (blue) for (b) and (d); -0.61 (red), yellow (0) to 0.61 (blue) for (c); and -0.37 (red), yellow (0) to 0.37 (blue) for the panel (e) in JOREK units.

While resistivity increase and ion-density decrease are connected in reality, they can be studied separately in our simulations. The drop in ion-density is executed via a negative volumetric source during the later 2D phase of the simulation, that causes a relatively smooth transition to a lower Deuterium ion-density before the switch is made to 3D.

Figure 8 shows the mode structure near the end of the linear phase for the different ion-density cases. It can be seen that the mode structure for ion-densities reduced to 50% and 15%, resemble closely that of the baseline scenario. That means a dominant 6/4 double tearing mode along with a 2/1 mode near the edge of the plasma (see figure 8). However, as the density is decreased further to 5%, the mode structure near the end of the linear phase involves dominance of both a 6/4 double tearing mode and a 2/1 tearing mode. Qualitatively, it mildly resembles what was observed in the high resistivity cases in the previous subsection (note that at large resistivity, we observed a pure 2/1 tearing mode to be dominant throughout).

Further evolution into the non-linear phase is marked by a relatively strong 2/1 tearing mode in all cases. This leads to stochasticization in the outer region, and a radially-inward expansion of stochasticity causing core-shrinking. This is accompanied by a near-complete RE current loss as shown in figure 9 for the cases with 15% and 5% ion-densities. Comparison of the evolution of 0D parameters are shown in figure 10. The remnant RE current as well as the RE loss

time are relatively lower at lower ion-densities as compared to that in the baseline scenario (see table 2). In general one can view the effect of Deuterium ion-density to be much weaker, but with qualitative resemblance to the effect of increased resistivity.

4.3. RE loads on first wall surface

As mentioned earlier, one of the goals of the benign termination scheme is to enhance the area of the RE footprint on the first wall. In order to estimate particle loads on the first wall surface during RE beam termination, the RE fluid model, in particular with field-parallel transport mimicked by parallel diffusion, is insufficient. Therefore the simulations were post-processed with a wall collision module in JOREK. In this module, kinetic particle markers are generated at the onset of the RE current drop and traced until they either collide with the wall or are lost outside of the simulation domain. For this purpose, we employ a CAD based 3D wall model of ITER constructed using a triangular mesh (since parts of the initial wall model lie outside of the simulation domain, the wall was shifted 10 centimeters down in the vertical direction to assure better overlap, while ensuring nearly no markers are lost).

The marker positions are sampled according to the starting RE number density profile obtained from the 3D RE fluid simulations. Furthermore, the distribution of particles

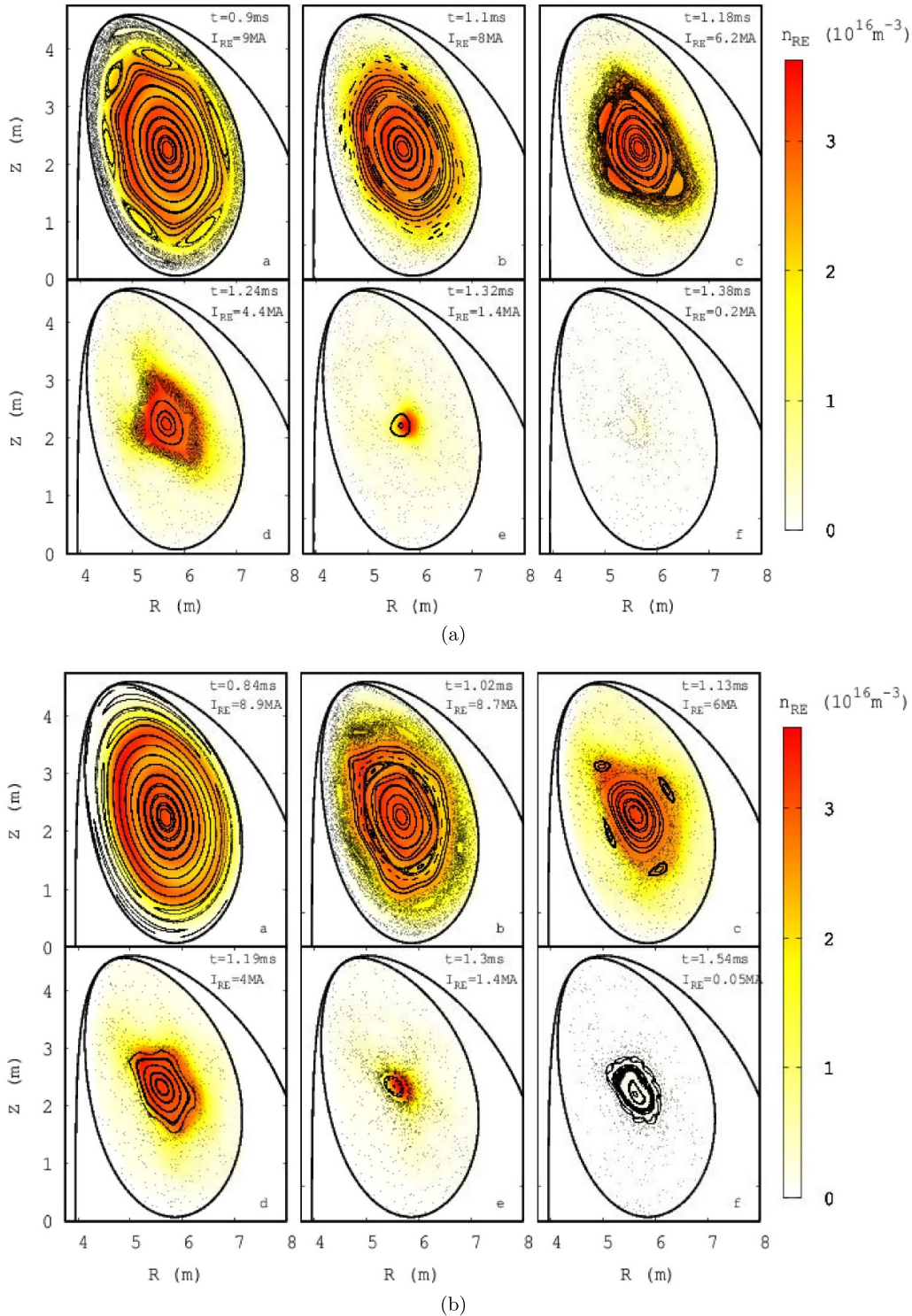


Figure 9. Poincaré plots over time for the termination cases with (a) $n_D^{\text{ion}} = 15\%$ case (T4b); (b) $n_D^{\text{ion}} = 5\%$ case (T4c). The color map represents the RE number density.

in momentum space is not known from the RE fluid simulations such that we assume all the RE particles have the same energy $E = 26 \text{ MeV}$ and pitch $|v_{\parallel}|/v = 0.99$. The choice of RE particle energy ensure that the total kinetic energy of all the RE particles ($\sim 24 \text{ MJ}$) was equivalent to the total magnetic energy channeled to REs as computed from the RE fluid simulation. Since we use a prescribed initial RE momentum

space distribution, acceleration by the electric field as well as the effects of collisions and radiation losses are not considered here. Furthermore, it is assumed that all the kinetic energy of the markers is deposited uniformly in each wall element (typical size of an element is $\sim 800 \text{ mm}^2$) upon collision. A total of 10^6 markers were used in these simulations. A detailed assessment of wall loads with different assumptions regarding RE

Table 2. Remnant RE current after the MHD crash, maximum MHD perturbation and the RE loss time for the various cases considered. RE loss time Δt_{RE}^{loss} refers to the time taken for RE current to drop from 80% to 20%.

Run	note	I_{RE}^{min} (kA)	$(\frac{dB}{B})^{max}$	Δt_{RE}^{loss} (ms)
T2a	Baseline	350	7.9%	0.54
T3a	$\eta = 3x$	26	14%	0.09
T3b	$\eta = 10x$	13	17.2%	0.06
T4a	$n_i^D = 50\%$	98	10%	0.25
T4b	$n_i^D = 15\%$	20	11.6%	0.18
T4c	$n_i^D = 5\%$	51	10.2%	0.19

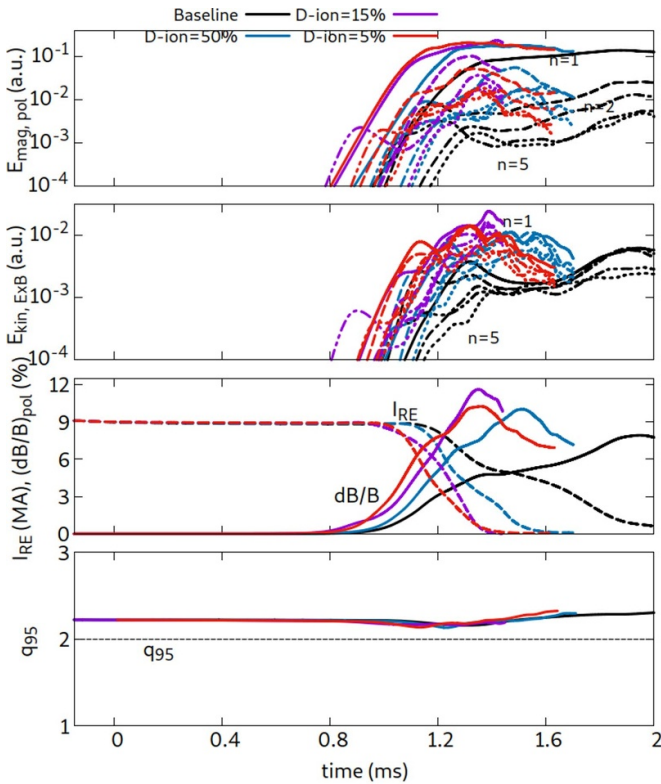


Figure 10. Comparison of global quantities for the terminations cases with different deuterium ion density. Baseline refers to Run T2a.

energies and pitch angles for different simulation scenarios will be published elsewhere including a detailed description of the virtual diagnostics [5].

Figure 11 shows the resulting energy load on the ITER first wall at the high field side for the baseline simulation case T2a. It can be seen that while the RE loads are mainly localized to three rows of tiles (poloidally), they also vary significantly in the toroidal direction, in some cases exceeding 10 MJ m^{-2} . The toroidal variation of the particle loads is more evident in figure 12(a), wherein the energy load is plotted with respect to the toroidal angle and the Z-coordinate along the wall contour, outlined in figure 12(b). Also shown in the latter figure is the locations where the REs collided with the wall, indicated by the red points. The pattern suggests that the dominant $n = 1$

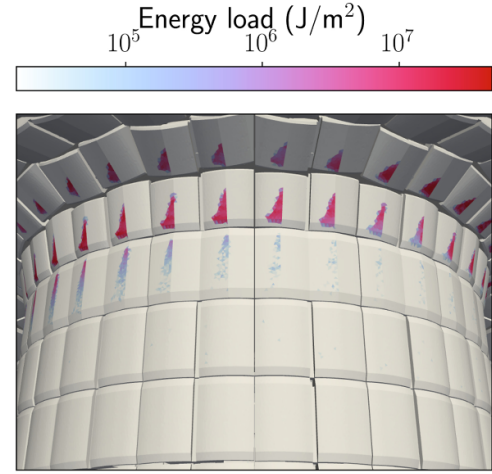


Figure 11. Energy load experienced by different wall elements on the wetted tiles at the high field side of ITER for simulation case T2a.

mode plays a significant role in how large the loads are able to grow, with the deposited energy differing by several orders of magnitude over a single period. For the lower row of tiles, located at $Z \sim 3 \text{ m}$, there also seems to be a more complex pattern emerging.

A summary of the peak and mean energy loads (over all of the affected wall elements) for all simulation cases is given in table 3. While the wall load distribution can depend on several factors such as initial RE distribution, strength of the different modes etc, the mean load decreases significantly at higher resistivity and to a much smaller extent at lower ion density. The mean energy load here refers to the average load when considering all wetted elements (since the surface is discretized using smaller elements, wetted area refers to the combined area of all elements where REs have collided).

It is important to consider the area over which the energy is distributed, which is shown in table 3. The most striking feature is the fact that the total affected area (or the wetted area) increases substantially when the resistivity is increased (in which case the stochastization was much stronger as discussed earlier). Such a clear trend though is not found when decreasing the ion density. It should be emphasized that the area exposed to very weak RE loads has been found to be sensitive to the number of markers used, and more computationally demanding simulations would be needed to provide more accurate predictions for those regions. As such, the total wetted area should most appropriately be viewed as a metric used to indicate trends in the broadness of the deposition. The regions exceeding the melt limit are however more well resolved due to the much larger sample of markers passing through each element. The melted area only accounts for the elements where the energy loads exceeded the melt limit of the wall material.

Previous work (L. Chen et al ‘Modeling runaway electron induced damage to ITER plasma-facing components’. In: 5th Asia Pacific Conference on Plasma Physics. Oct. 19, 2021) has indicated that the melt limit of the beryllium tiles lie around

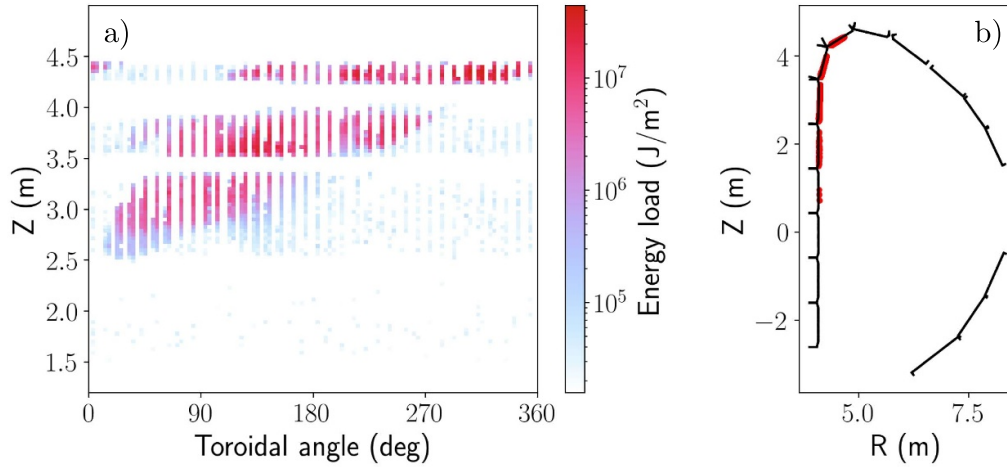


Figure 12. (a) Energy load experienced by wall elements as a function of toroidal angle and Z-coordinate along the contour of the wall outlined in (b) together with the location of the RE collisions indicated in red.

Table 3. Summary of the peak and mean energy loads obtained for the different simulation cases. Wetted area is the combined area of all surface elements where REs have collided, while the melted area included all elements where the energy loads exceeded the melt limit.

Run	comment	$W_{\text{wall}}^{\text{max}}$ (MJ m^{-2})	$W_{\text{wall}}^{\text{mean}}$ (MJ m^{-2})	A_{wetted} (m^2)	A_{melted} (m^2)
T2a	Baseline	48	4.7	4.9	0.50
T3a	$\eta = 3x$	45	2.7	9.4	0.37
T3b	$\eta = 10x$	34	2.1	12.6	0.37
T4a	$n_{\text{ion}}^D = 50\%$	58	3.8	6.3	0.43
T4b	$n_{\text{ion}}^D = 15\%$	53	3.9	6.3	0.49
T4c	$n_{\text{ion}}^D = 5\%$	54	3.6	6.6	0.46

$\sim 14 \text{ MJ m}^{-2}$. The maximum loads obtained in each of the cases is notably more than this limit, which might be of concern in relation to the integrity of the cooling channels in ITER. The area over which the loads are larger than the melt limit is shown in the last column of table 3. Increase in the total wetted area at larger resistivity also comes with a notable reduction of the area exposed to a heat load of more than 14 MJ m^{-2} . It drops by around 26% as a consequence of the resistivity increase by a factor 3. In the case of lower ion-densities the change is more subtle and no clear trend is observed.

5. Summary and discussion

First 3D non-linear MHD simulations of RE beam termination scenarios in ITER have been presented as obtained with the RE fluid model in the JOREK code. The plasma state considered for termination simulations had a mildly hollow current profile and an edge safety factor around a value of 2. In all cases, both the low edge safety factor as well as the hollow current profile contribute to growth of MHD instabilities, eventually leading to a stochastic magnetic field. The associated fast parallel transport of REs in the stochastic field leads to a near-complete loss of RE current. Robustness of the observation is rather encouraging (if we can ensure negligible re-avalanching

via 2nd D injection etc) in the context of a potential risk posed by RE beams in ITER.

The possible benefits of a second Deuterium injection into the RE beam to induce benign termination have been assessed by varying the plasma resistivity and the ion density during the termination phase. In the context, the effects of higher electrical resistivity and lower Deuterium ion-densities were studied separately. At higher resistivity, much larger MHD magnitudes along with stronger stochastic states and less remnant REs are observed. There is a marked dominance of the 2/1 tearing mode at higher resistivities throughout the evolution (linear and non-linear phases). This can be attributed to the lack of a 3/2 mode induced stochasticization in the outer region, which was present in the baseline scenario. The effect of lowering the Deuterium ion-density however showed a much weaker effect, albeit qualitatively tending towards the theme observed at higher resistivity. In either case, the much faster and stronger RE losses are potentially advantageous.

Finally, RE load distributions on the first wall have been assessed. Strong poloidal localization as well as a large variation in the toroidal direction is observed, in line with the dominant MHD mode. A key result has been the observation of a strong increase in the spread of RE loads at higher resistivity, markedly for the lower energy densities. Such a clear trend though is not found when the ion density was decreased.

The peak energy load was seen to decrease for the higher resistivity cases whereas for lower ion-densities there was even a moderate increase. Over all the simulations done here, the area over which the load exceeded the Beryllium melt limit of 14 MJ m^{-2} varied between 0.37 m^2 to 0.50 m^2 .

Due to computational constraints in performing long time-scale 3D simulations starting from RE plateau phase, the scope of this work was limited to the standalone study of RE beam termination scenarios when $q_{95} \sim 2$ is obtained. Nevertheless, the scenarios studied here are very plausible and provide valuable insights (both qualitative and quantitative) on the nature of RE beam termination in ITER. The remnant RE current after termination is significantly larger than typical RE seeds and has the potential to re-avalanche. At the same time, one would have flux-surface reformation, continued stochastic RE losses and plasma scraping. It is important to understand whether the interplay of the aforementioned processes can lead to a re-formation of a multi-MA RE beam. Studies in that direction will follow in the future.

There are several possible avenues to further improve the predictive capability for RE impact in ITER. Inclusion of the effect of enhanced scattering (and ionization) by REs, orbit shifted RE equilibrium, two/three temperature models, starting from a more stable plasma state, cases with smaller RE current etc are some of the avenues that the authors plan to study in the near future. It must be noted that *predicted* post-TQ current density and RE seed profiles are essential towards truly predictive simulations for RE impact in ITER. This requires realistic 3D MHD simulations of the thermal quench in ITER, on which efforts are on-going (e.g. [16]). Such simulations should in addition be also coupled to a kinetic treatment of REs, which is also an ongoing effort [4]. More extensive kinetic simulations over the complete beam formation period using e.g. particle tracing or flux-surface averaging could be conducted in order to obtain more appropriate estimates for the momentum space distribution of these particles.

Acknowledgment

The authors acknowledge fruitful discussions with E Nardon (CEA). We also acknowledge help from Gregor Simic (ITER Organization) via sharing ITER first-wall panel geometry. This work has been carried out within the framework of the ITER implementing Agreement No.3, Ref:IO/IA/20/4300002200. Part of this work was supported by the EUROfusion-Theory and Advanced Simulation Coordination (E-TASC) via the theory and simulation verification and validation (TSVV) projects on MHD transients and REs in disruptions (2021–2025). Part of this work has been carried out within the framework of the EUROfusion Consortium, funded by the European Union via the Euratom Research and Training Programme (Grant Agreement No. 101052200 of EUROfusion). Views and opinions expressed are however those of the author(s) only and do not necessarily reflect those of the European Union or the European Commission. Neither the European Union nor the European

Commission can be held responsible for them. ITER is the Nuclear Facility INB No. 174. This work explores the physics processes during plasma operation of the tokamak when disruptions take place; nevertheless the nuclear operator is not constrained by the results presented here. The views and opinions expressed herein do not necessarily reflect those of the ITER Organization.

ORCID iDs

M. Hoelzl  <https://orcid.org/0000-0001-7921-9176>

H. Bergström  <https://orcid.org/0009-0004-6274-1661>

M. Lehnen  <https://orcid.org/0000-0001-6043-8803>

References

- [1] Artola F.J., Loarte A., Hoelzl M., Lehnen M. and Schwarz N. (the JOEUK Team) 2022 Non-axisymmetric MHD simulations of the current quench phase of ITER mitigated disruptions *Nucl. Fusion* **62** 056023
- [2] Bandaru V., Hoelzl M., Artola F.J., Papp G. and Huijsmans G.T.A. 2019 Simulating the nonlinear interaction of relativistic electrons and tokamak plasma instabilities: implementation and validation of a fluid model *Phys. Rev. E* **99** 063317
- [3] Bandaru V., Hoelzl M., Reux C., Ficker O., Silburn S., Lehnen M. and Eidietis N. (JOEUK Team and JET Contributors) 2021 Magnetohydrodynamic simulations of runaway electron beam termination in JET *Plasma Phys. Control. Fusion* **63** 035024
- [4] Bergström H. and Hoelzl M. 2023 Disruption and runaway electron modeling with JOEUK *Poster in the Theory and Simulation of Disruptions Workshop*
- [5] Bergström H., Särkimäki K. and Bandaru V. 2024 Assessment of the runaway electron load distribution in ITER during 3D MHD induced beam termination (in preparation)
- [6] Breizman B.N., Aleynikov P., Hollmann E.M. and Lehnen M. 2019 Physics of runaway electrons in tokamaks *Nucl. Fusion* **59** 083001
- [7] Czarny O. and Huysmans G.T.A. 2008 Bezier surfaces and finite elements for MHD simulations *J. Comput. Phys.* **227** 7423–45
- [8] Furth H.P., Killeen J.P. and Rosenbluth M.N. 1963 Finite-resistivity instabilities of a sheet pinch *Phys. Fluids* **6** 459
- [9] Gorbunov E.P. and Razumova K.A. 1964 Effect of a strong magnetic field on the magnetohydrodynamic stability of a plasma and the confinement of charged particles in the tokamak machine *J. Nucl. Energy C* **6** 515–25
- [10] Hender T.C. et al (the ITPA MHD, Disruption and Magnetic Control Topical Group) 2007 Disruption and magnetic control topical group 2007 chapter 3: MHD stability, operational limits and disruptions *Nucl. Fusion* **47** S128
- [11] Hesslow L., Embréus O., Stahl A., DuBois T.C. and Papp G. 2017 Effect of partially screened nuclei on fast-electron dynamics *Phys. Rev. Lett.* **118** 255001
- [12] Hesslow L., Embréus O., Wilkie G.J., Papp G. and Fülöp T. 2018 Effect of partially ionized impurities and radiation on the effective critical electric field for runaway generation *Plasma Phys. Control. Fusion* **60** 074010
- [13] Hoelzl M., Huijsmans G.T.A., Pamela S.J.P., Becoulet M., Nardon E., Artola F.J. and Nkonga B. 2021 The JOEUK non-linear extended MHD code and applications to

- large-scale instabilities and their control in magnetically confined fusion plasmas *Nucl. Fusion* **61** 065001
- [14] Hoelzl M., Merkel P., Huysmans G.T.A. and Nardon E. 2012 Coupling JOREK and STARWALL codes for non-linear resistive-wall simulations *J. Phys.: Conf. Ser.* **401** 012010
- [15] Hollmann E.M., Baylor L., Boboc A. and Carvalho P. 2023 Trends in runaway electron plateau partial recombination by massive H₂ or D₂ injection in DIII-D and JET and first extrapolations to ITER and SPARC *Nucl. Fusion* **63** 036011
- [16] Hu D., Nardon E., Artola F.J. and Lehnen M. 2023 Collisional-radiative simulation of impurity assimilation, radiative collapse and MHD dynamics after ITER shattered pellet injection *Nucl. Fusion* **63** 066008
- [17] Huysmans G.T.A. and Czarny O. 2007 MHD stability in X-point geometry: simulation of ELMs *Nucl. Fusion* **47** 659
- [18] Liu C., Zhao C., Jardin S.C. and Ferraro N.M. 2021 Self-consistent simulation of resistive kink instabilities with runaway electrons *Plasma Phys. Control. Fusion* **63** 125031
- [19] Martín-Solís J.R., Loarte A. and Lehnen M. 2017 Formation and termination of runaway beams in ITER disruptions *Nucl. Fusion* **57** 066025
- [20] Matsuyama A., Aiba N. and Yagi M. 2017 Reduced fluid simulation of runaway electron generation in the presence of resistive kink modes *Nucl. Fusion* **57** 066038
- [21] Matthews G.F., Bazylev B. and Baron-Wiechec A. 2016 Melt damage to the JET ITER-like wall and divertor *Phys. Scr.* **T167** 014070
- [22] Merkel P. and Sempf M. 2006 Feedback stabilization of resistive wall modes in the presence of multiply connected wall structures *IAEA Fusion Energy Conf.* p TH/3-8
- [23] Nardon E., Bandaru V., Hoelzl M., Artola F.J. and Maget P. (JOREK Team and JET Contributors) 2023 Non-linear dynamics of the double tearing mode *Phys. Plasmas* **30** 092502
- [24] Nygren R., Lutz T., Walsh D., Martin G., Chatelier M., Loarer T. and Guilhem D. 1997 Runaway electron damage to the Tore Supra Phase III outboard pump limiter *J. Nucl. Mater.* **241–243** 522–7
- [25] Paz-Soldan C., Liu Y., Reux C. and Del-Castillo-Negrete D. 2021 A novel path to runaway electron mitigation via Deuterium injection and current-driven kink instability *Nucl. Fusion* **61** 116058
- [26] Reux C., Paz-Soldan C., Aleynikov P., Bandaru V. and Ficker O. (JET Contributors) 2021 Runaway electron beam suppression using impurity flushing and large magnetohydrodynamic instabilities *Phys. Rev. Lett.* **126** 175001
- [27] Reux C., Plyusnin V., Alper B. and Alves D. 2015 Runaway electron beam generation and mitigation during disruptions at JET-ILW *Nucl. Fusion* **55** 093013
- [28] Sheikh U., Cazabonne J., Cerovsky J. and Coda S. 2022 Benign Termination of Runaway Electron Beams on ASDEX Upgrade and TCV *Talk Presented at the IAEA Technical Meeting on Disruptions*
- [29] Vallhagen O., Embreus O., Pusztai I., Hesslow L. and Fülöp T. 2020 Runaway dynamics in the DT phase of ITER operations in the presence of massive material injection *J. Plasma Phys.* **86** 475860401
- [30] Waddell B.V., Carreras B., Hicks H.R. and Holmes J.A. 1979 Nonlinear interaction of tearing modes in highly resistive tokamaks *Phys. Fluids* **22** 896–910